

Electrical Detection of Individual Skyrmions in Graphene Devices

F. Finocchiaro¹, J. L. Lado² and J. Fernandez-Rossier^{2,3}

¹*IMDEA Nanociencia, Calle de Faraday 9, Cantoblanco 28049 - Madrid, Spain*

²*QuantaLab, International Iberian Nanotechnology Laboratory (INL),
Av. Mestre Jose Veiga, 4715-310 Braga, Portugal and*

³*Departamento de Física Aplicada, Universidad de Alicante, San Vicente del Raspeig, 03690 Spain*

(Dated: November 28, 2021)

We study a graphene Hall probe located on top of a magnetic surface as a detector of skyrmions, using as working principle the anomalous Hall effect produced by the exchange interaction of the graphene electrons with the non-coplanar magnetization of the skyrmion. We study the magnitude of the effect as a function of the exchange interaction, skyrmion size and device dimensions. Our calculations for multiterminal graphene nanodevices, working in the ballistic regime, indicate that for realistic exchange interactions a single skyrmion would give Hall voltages well within reach of the experimental state of the art. The proposed device could act as an electrical transducer that marks the presence of a single skyrmion in a nanoscale region, paving the way towards the integration of skyrmion-based spintronics and graphene electronics.

I. INTRODUCTION

Skyrmions are magnetic non-coplanar spin textures that are attracting a great deal of attention for both their appealing physical properties¹ and their potential use in spintronics^{2–5}. They have been observed forming lattices in a variety of non-centrosymmetric magnetic crystals^{6–9}, including insulating materials such as the chiral-lattice magnet Cu_2OSeO_3 ^{10–12}. They also form two dimensional arrays in atomically thin layers of Fe deposited on Ir(111)^{13,14}. In these systems the spins typically feel a competition between aligning with their neighbors and being perpendicular to them, what favors chiral ordering. A variety of interactions can assist non-collinear arrangements, including Dzyaloshinskii-Moryia interactions, dipolar interactions and frustrated exchange interactions and the size of an individual skyrmion can range from 1 nm to 1 μm depending on which specific mechanism is involved. To date, these magnetic structures are detected by means of neutron scattering⁶, electron microscopy¹⁵ and even individually, with atomic scale resolution, by means of spin polarized scanning tunneling microscopy^{13,16} and atomic size sensors¹⁷.

The particle-like nature of skyrmions has motivated proposals to use them as elementary units to store classical digital information, inspired by the magnetic domain-wall racetrack memories¹⁸. Such a perspective has become increasingly attractive since it has been experimentally proved¹⁴ the possibility of manipulating two-dimensional magnetic lattices by creating and destroying individual skyrmions by means of spin-polarized currents in STM devices. This, along with the experimental finding¹⁹ of skyrmion motion driven by ultralow current densities of the order of 10^{-6} A m^{-2} , considerably smaller than those needed for domain wall motion in ferromagnets, makes skyrmions potentially optimal candidates for the next generation of magnetoelectronic read-out devices.

Mathematically, skyrmions are topologically non-trivial objects whose topology content is embedded in

an index, the winding number N , defined as

$$N = \frac{1}{4\pi} \int_A \mathbf{n}(x, y) \cdot \left(\frac{\partial \mathbf{n}(x, y)}{\partial x} \times \frac{\partial \mathbf{n}(x, y)}{\partial y} \right) dx dy \quad (1)$$

where $\mathbf{n}(x, y) : \mathbb{R}^2 \rightarrow \mathbb{R}^3$ is a classical magnetization field and the two-dimensional integral is performed over the overall area occupied by the skyrmion. The winding number N can only acquire integer values, and a skyrmion is distinguished from other topologically trivial magnetic textures for exhibiting a non-zero value of the integer N . The magnetization field $\mathbf{n}(x, y)$ of a skyrmion can be expressed as a mapping from the polar plane coordinates $\mathbf{r} = (r, \phi)$ to the unit sphere coordinates (Φ, Θ)

$$\mathbf{n}(\mathbf{r}) = (\cos \Phi(\phi) \sin \Theta(r), \sin \Phi(\phi) \sin \Theta(r), \cos \Theta(r)) \quad (2)$$

provided the spin configuration at $r = \infty$ is ϕ -independent so that it can be mapped to a single point on the sphere. The mapping is specified by the two functions²⁰:

$$\Phi(\phi) = N\phi + \gamma \quad (3)$$

and $\Theta(r)$ varies from 0 for large r to π as we approach $r = 0$, the core of the skyrmion. Here we adopt the following model:

$$\Theta(r) = \begin{cases} \pi & \text{for } r = 0 \\ f(r) = \pi(1 - r/R) & \text{for } 0 < r \leq R \\ 0 & \text{for } r > R \end{cases} \quad (4)$$

where N is the skyrmion winding number introduced in (1), γ is a phase termed helicity that can be gauged away by rotation around the z -axis, and $f(r) = \pi(1 - r/R)$ is a function of the radial coordinate that describes a smooth radial profile inside of the skyrmion radius R . Such a texture describes a magnetic configuration where the spins are all aligned perpendicular to the film plane with the exception of those comprised within the radius R where they all progressively align along the anti-parallel

direction, that is picked up exactly at $r = 0$. The condition that the spins at $r = 0$ and $r = \infty$ are oppositely oriented is crucial in order to ensure a non-trivial topology of the magnetic texture.

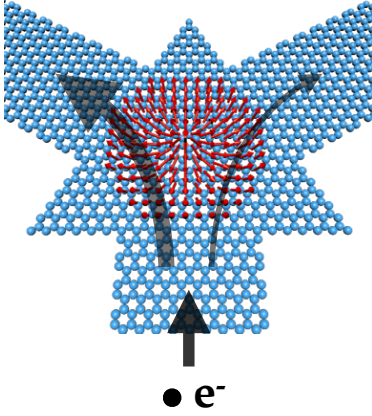


Figure 1. A graphene triangular quantum dot (the transmission region) proximized with a skyrmion and connected to three leads. Due to the anomalous Hall effect, a net transverse voltage is generated by the skew scattering of Dirac electrons traveling through the central region.

Several recent theoretical works^{21–23} point out that two-dimensional systems coupled either weakly or strongly to individual skyrmions or skyrmionic lattices can develop an Anomalous Hall (AH) or Quantum Anomalous Hall (QAH) phase owing to the non-trivial topology of these structures in real space. This effect refers to the onset of a transverse Hall response arising in magnetic systems driven by anomalous velocities, associated to Berry curvature, without the need of an applied magnetic field²⁴. This anomalous Hall response can be either of extrinsic or intrinsic nature. In the case of proximizing a pristine 2D system with magnetic skyrmions, the generation of a transverse voltage is of extrinsic nature and ascribable to the imprinting of the skyrmions real space topology onto the (trivial) reciprocal space topology of the non-magnetic system²³. Based on these findings, along with a recent work demonstrating the possibility of growing a graphene flake on top of a single atomic layer of Fe on a Ir(111) substrate^{21,25}, here we consider graphene flakes weakly coupled to magnetic films as skyrmion detectors. To this aim, we compute the skewness of the scattering and the associated Hall signal induced in a graphene island coupled to a single skyrmion within a multi-terminal geometry. Graphene unique properties are ideal to implement the proposed device. As a fact, being atomically thin maximizes proximity effects, making it an optimal material to grow on top of magnetic materials. Furthermore, the fabrication of high quality graphene electronic devices both at the micron and nanometer scale is absolutely well demonstrated^{26–28} and its use as a magnetic sensor for magnetic adsorbates has been already tested experimentally^{29,30} and studied

theoretically³¹.

The paper is organized as follows. In section II we discuss a 2D Dirac system in the continuum coupled to a non-uniform spin texture and performing a standard rotation in spin space we unveil two types of influence on the Dirac electrons. In section III we introduce Landauer's formalism for quantum transport on the lattice and describe the setup of the proposed Hall experiment. Finally, in section IV, we discuss the results obtained by applying Landauer's formula to a graphene flake coupled to a single skyrmion, characterizing the Hall conductance as a function of several parameters and comparing the effectiveness of graphene with that of a standard two-dimensional electron gas (2DEG).

II. ANALYTIC APPROACH IN THE CONTINUUM

In this section we describe graphene electrons interacting with a non-coplanar magnetization field \mathbf{n} , as given by equation (2), using a 2D Dirac Hamiltonian:

$$H = H_0 + H_{ex} = -i\hbar\tau v_F (\partial_x \sigma_x + \tau \partial_y \sigma_y) + J \mathbf{n} \cdot \mathbf{s} \quad (5)$$

with $\mathbf{s} = (s_x, s_y, s_z)$ the vector of Pauli matrices acting in spin space and $\boldsymbol{\sigma} = (\sigma_x, \sigma_y, \sigma_z)$ the vector of Pauli matrices acting in pseudo-spin space. We perform a rotation of the Hamiltonian so that in every point of space the spin quantization axis is chosen along the direction of the spin texture \mathbf{n} . As a result, the representation of the exchange term is diagonal in the rotated frame, but the Dirac Hamiltonian acquires new terms that encode the influence of the exchange interaction of the Dirac electrons with the non-coplanar field. The unitary matrix \mathcal{R} that performs such a transformation in the basis $\psi = (A \uparrow, B \uparrow, A \downarrow, B \downarrow)^T$ is

$$\mathcal{R} = \begin{pmatrix} u & 0 & v & 0 \\ 0 & u & 0 & v \\ -v^* & 0 & u^* & 0 \\ 0 & -v^* & 0 & u^* \end{pmatrix} = \begin{pmatrix} u & v \\ -v^* & u^* \end{pmatrix} \otimes \sigma_0 \quad (6)$$

where

$$u = \cos \frac{\Theta(r)}{2} e^{i\Phi(\phi)/2} \quad v = \sin \frac{\Theta(r)}{2} e^{-i\Phi(\phi)/2} \quad (7)$$

The transformed Hamiltonian $H \rightarrow H' = \mathcal{R} H \mathcal{R}^{-1}$ reads

$$H' = \tau v_F [\sigma_x (p_x + \mathcal{A}_x) + \tau \sigma_y (p_y + \mathcal{A}_y)] + \frac{\hbar \tau v_F}{2} \left[-\sigma_x \left(\frac{N}{r} s_x n_y + \partial_r \theta s_y \cos \phi \right) + \tau \sigma_y \left(\frac{N}{r} s_x n_x - \partial_r \theta s_y \sin \phi \right) \right] + J s_z \quad (8)$$

with

$$\begin{aligned} \mathcal{A}_x &= \hbar \frac{N}{2r} \cos \theta \sin \phi \otimes s_z \\ \mathcal{A}_y &= -\hbar \frac{N}{2r} \cos \theta \cos \phi \otimes s_z \end{aligned} \quad (9)$$

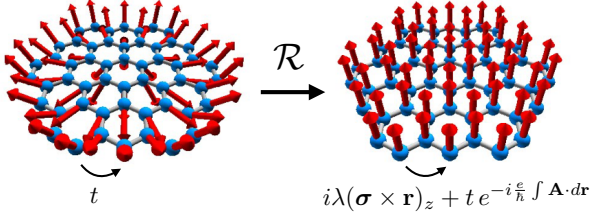


Figure 2. Mapping of a system characterized by real hopping and with a double exchange interaction with a non-coplanar magnetic texture to a system with spatially uniform magnetization field and with a complex hopping function mimicking the coexistence of spin-orbit with a vector gauge field.

and $n_x = \cos \Phi \sin \Theta$, $n_y = \sin \Phi \sin \Theta$. In the rotated reference frame, the exchange term is manifestly diagonal. Besides, the Hamiltonian has acquired additional kinetic terms. The $\mathcal{A} = (\mathcal{A}_x, \mathcal{A}_y)$ field acts as a spin-dependent gauge vector potential that couples with the momenta of the Dirac electrons, whereas the remaining two terms closely resemble a spin-orbit (SO) interaction of the Rashba type. On the lattice, this corresponds to mapping a system characterized by a non-collinear exchange field and real hopping to a ferromagnetic system with a purely imaginary hopping mimicking the effect of SO coupling plus a complex hopping supported by a gauge field entering as a Peierls phase. This is schematized in figure 2. From the gauge field, one can compute the effective magnetic field acting on the system as

$$\mathcal{B} = \nabla \times \mathcal{A} = \hbar \frac{N}{2r} s_z \left[\partial_r \theta \sin \theta - \frac{1}{r} \cos \theta \right] \hat{z} \quad (10)$$

that reads

$$\mathcal{B}_z = -\hbar \frac{N}{2r} s_z \begin{cases} \left[\pi \sin \theta / R + r^{-1} \cos \theta \right] & \text{for } r \leq R \\ r^{-1} & \text{for } r > R \end{cases} \quad (11)$$

This transformation of the Hamiltonian therefore allows to interpret the topological content embedded in the skyrmion texture as a superposition of two effects: (i) The generation of an effective emergent electromagnetic field (EEMF) described by the gauge potential \mathcal{A} ; (ii) The coexistence of ferromagnetic exchange with a Rashba-like SO interaction, what has been predicted to give rise to a QAH phase³². Both ingredients are endowed with a topological character that the skyrmion texture is able to imprint onto the Dirac electrons and are therefore responsible for generating a Hall response in the system. An analog result has been derived⁷ for Schrodinger electrons, with the remarkable difference that in the strong coupling limit ($J \gg t$) the spin-mixing terms vanish and the problem is exactly mapped to a spinless one-band system where the electrons momenta are coupled to a vector potential describing an emergent magnetic field. In the case of Dirac electrons, the spin-mixing term survives at all coupling regimes and the mapping to a pure EEMF is an incomplete description of

the physics taking place in the system. Whereas this picture provides some physical insight of what happens to graphene Dirac electrons surfing a skyrmions, it does not provide a straightforward method to compute the Hall response.

III. TIGHT-BINDING QUANTUM TRANSPORT APPROACH

In this section we overview the quantum transport methodology that we will employ to compute the Hall response induced by an individual magnetic skyrmion in a graphene device. Importantly, we are implicitly assuming that the substrate material is an insulating skyrmion crystal such as CuGeO_3 ³³ and Cu_2OSeO_3 ^{10–12} in such a way that the current only flows through graphene.

The graphene electrons are described with the standard tight-binding Hamiltonian for the honeycomb lattice with one p_z orbital per atom³⁴, plus their exchange interaction with the classical magnetization of the skyrmion \mathbf{n} :

$$H = -t \sum_{\langle i,j \rangle, \sigma} c_{i\sigma}^\dagger c_{j\sigma} + J \sum_i \mathbf{S}_i \cdot \mathbf{n}_i \quad (12)$$

Here \mathbf{n}_i is the classical continuous magnetization texture (2) discretized over the graphene lattice and taken at site i and $\mathbf{S}_i = \sum_{\sigma\sigma'} c_{i\sigma}^\dagger \mathbf{s}_{\sigma\sigma'} c_{i\sigma'}$ is the vector whose components are the Pauli matrices acting in spin space associated with the i -th lattice site. The $\langle i, j \rangle$ symbol implies summation over all nearest neighboring pairs of atoms, and we are assuming that the magnitude of the magnetization is uniform over the whole graphene lattice. This Hamiltonian has been considered before²³ for the case of 2D graphene interacting with a skyrmion crystal. In contrast, here we consider a graphene device that hosts an individual skyrmion.

The mathematical framework that we use to study quantum transport is based on Landauer's formalism for conductance³⁵. Given an experimental setup where a device is attached to N metallic contacts, Landauer's multi-terminal technique allows to compute the transmission amplitude between the m -th and the n -th contact from the relation

$$T_{mn} = \text{Tr} (G_d^+ \Gamma_n G_d \Gamma_m) \quad (13)$$

where G_d and G_d^+ are respectively the retarded and advanced Green's functions of the device, that is the Green's function of the isolated device corrected by the self-energies Σ_m of the N leads

$$G_d(\epsilon) = \left[(\epsilon + i\delta) \mathbb{I} - H_d - \sum_{m=0}^{N-1} \Sigma_m \right]^{-1} \quad (14)$$

where H_d is the Hamiltonian of the isolated device. The Γ_m 's are quantities associated to the leads' selfenergies

as $\Gamma_m = i(\Sigma_m - \Sigma_m^+)$. The leads' self-energies incorporate the coupling between the device and the leads as $\Sigma_m = t_m^+ g_m t_m$, with g_m the surface Green's function³⁶ of the m -th lead, and t_m the hopping matrix between the device and the m -th lead. From the knowledge of the transmission amplitudes, the expression for the total current flowing from the lead m follows straightforwardly:

$$I_m = \frac{e}{h} \sum_{n \neq m} \int_{-\infty}^{+\infty} d\epsilon [f(\epsilon - \mu_m) - f(\epsilon - \mu_n)] T_{mn}(\epsilon) \quad (15)$$

with $f(\epsilon - \mu)$ the Fermi distribution function, so that at zero temperature the previous expression reduces to $I_m = \frac{e}{h} \sum_{n \neq m} \int_{\mu_n}^{\mu_m} d\epsilon T_{mn}(\epsilon_F)$ and for a sufficiently small energy interval $\mu_m - \mu_n$ one can expand the transmission coefficient $T_{mn}(\epsilon)$ around the Fermi energy ϵ_F and stick to zeroth order. By doing so, one finally finds that the formula for the current flowing from the lead m becomes:

$$I_m = \frac{e}{h} \sum_{n \neq m} (\mu_m - \mu_n) T_{mn}(\epsilon_F) \quad (16)$$

This equation can be used to derive the Hall response in a given multiterminal device in two different ways. In both cases, the first step of the calculation is the numerical determination of the transmission coefficients $T_{mn}(\epsilon)$. Then we can either impose (i) the voltage drops eV , defined as the difference between the chemical potentials of the different electrodes, and compute the resulting current (inverse Hall effect), or (ii) impose a longitudinal current flow and a null transverse current, find the resulting chemical potentials and determine the Hall response (direct Hall effect).

When the methods just described are implemented in an ordinary four-terminal geometry²², the resulting relation between the Hall conductance and the transmission coefficients is far from intuitive. In this paper, for the sake of simplicity, we consider a three terminal device (TTD) of the kind of the one shown in figure 3a. We choose to fix the chemical potentials of the three electrodes, labeled as 0, 1 and 2, and compute the resulting current. Specifically, we impose that $V_0 = V$ and $V_1 = V_2 = -V$. In this way, the voltage difference between leads 1 and 2 is automatically set to zero whereas the voltage difference between lead 0 and leads 1,2 is $V_y = V_0 - V_{1,2} = 2V$. The expression for the current flowing from leads 1 and 2 is $I_i = 2VT_{0i}$ for $i = 1, 2$. From this expressions it is straightforward to deduce the current imbalance δI , that reflects the presence of a transverse force, $\delta I = I_1 - I_2 = 2V(T_{01} - T_{02})$, whence our definition of Hall conductance in this geometry

$$G_H = \frac{\delta I}{V_0 - V_{1,2}} = \frac{e^2}{h} (T_{01} - T_{02}) \equiv \frac{e^2}{h} \delta T \quad (17)$$

In the following we present the numerical results for the normalized transmission imbalance, that is

$$\mathcal{T} = \frac{\delta T}{T} \equiv (T_{01} - T_{02}) / (T_{01} + T_{02}) \quad (18)$$

in order to work with quantities that do not depend on the number of conduction channels in the device. This 3-terminal setup simplifies considerably the analysis of the numerical results, and also matches the C_3 symmetry of the graphene lattice. However, in a real device, disorder and contact asymmetries might result in additional transmission imbalances that might obscure the detection of skyrmions. Thus, in real devices a standard 4 terminal geometry should be used, given that the principles and magnitude of the physical effect are expected to be the same.

IV. RESULTS AND DISCUSSION

We now present the results obtained by calculating the imbalance in the transmission coefficients \mathcal{T} eq. (18) for a graphene quantum dot coupled to a skyrmion. For a better physical insight, we provide an estimate for the *equivalent* magnetic field B_{eq} that would give rise to a conventional Hall response of the same magnitude of that induced by the skyrmion. Details on the determination of such a field are given in the Appendix. In the following we consider flakes sizes of the order of ~ 50 nm², and skyrmions with radius of the order of 2-3 nm and winding number $N = 1$. Also, we are solely interested in realistic^{37,38} weak exchange proximity effects, that do not alter the graphene spectrum substantially, so we explore coupling constants up to $J \sim 100$ meV³⁹. In order to simulate standard metallic contacts in some of the calculations square leads have been used instead of hexagonal leads. Results obtained with different leads geometries are consistent, so we chose to present curves associated to one or the other geometry in order to minimize resonance effects due to confinement inside of the central island.

A. Anomalous Hall effect

We first investigate the magnitude and behavior of the transmission asymmetry \mathcal{T} as a function of the coupling constant J , comparing the results for Dirac electrons (half filled honeycomb lattice), and Schrodinger electrons (heavily doped honeycomb lattice). The result is shown in fig. 3(b) in both linear and logarithmic scale, for a skyrmion with radius $R = 2.3$ nm and a device of linear dimension $L = 10.6$ nm. The first thing to notice is that, even for small $J \simeq 1$ meV, the equivalent field B_{eq} is of the order of 1 Tesla, which shows that the anomalous Hall effect is very large. For $J < 100$ meV the transmission imbalance \mathcal{T} of Dirac electrons shows an approximately linear behavior with J in contrast with the case of Schrodinger electrons (Fermi energy away from the Dirac point) for which $\mathcal{T} \propto J^3$. For all the values of J , the Hall response for Dirac electrons is much larger than for Schrodinger electrons, most notably for the experimentally relevant case of small J , for which \mathcal{T} is up

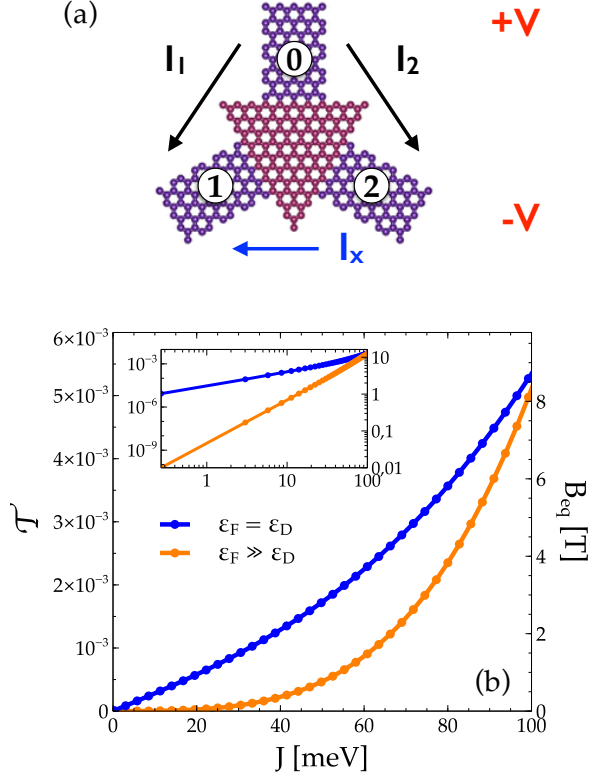


Figure 3. (a) Three terminal device setup for the inverse Hall measurement with C_3 rotational symmetry. (b) Normalized transmission imbalance \mathcal{T} (eq. 18) and equivalent magnetic field B_{eq} as a function of the coupling constant J , comparison of a Dirac-like (undoped graphene) and a Schrodinger-like (heavily doped graphene) material for an island with side of 10.6 nm and a skyrmion radius of 2.3 nm. Inset: log-log representation of $\mathcal{T}(J)$ and $B_{eq}(J)$.

to 4 orders of magnitude larger. This difference is reduced and eventually canceled at higher and unrealistic couplings larger than 100 meV.

We now characterize the Hall conductance of a graphene TTD by investigating its dependence on the system parameters, such as the Fermi energy of the leads, the skyrmion size R and the size of the graphene island coupled to the skyrmion. The results are shown in fig. 4. The anomalous Hall response as a function of the chemical potential of graphene (fig. 4(a,b)), shows a local maxima at charge neutrality, and other two local maxima of opposite sign at symmetric electron/hole doping, a behavior resembling graphene coupled to a skyrmion crystal.²³ Such phenomenology can be understood in terms of the modification of the Dirac cone due to the non-coplanar magnetization field. As we have seen in section II, the problem can be mapped to one where spatially uniform exchange field and Rashba-like spin-mixing terms coexist. The first contribution has the effect of lifting spin degeneracy, whereas the latter opens small gaps at both the Fermi energy and at crossing points forming

at higher energies of the order of $\pm J$. Within these gaps, the absolute value of the Berry curvature reaches local maxima and this is reflected in the behavior of \mathcal{T} as a function of the transmission energy ε shown in fig. 4.

In fig. 4(c) we show the behavior of \mathcal{T} as a function of the skyrmion radius R , keeping the dimension of the device constant and equal to $L = 10.6$ nm, and $J = 80$ meV. We consider the case of small skyrmions with nanometric radius such as those found in systems with frustrated exchange interactions⁴⁰. Two competing effects are at play as the radius of the skyrmion increases: on the one side the change in magnetization as a function of the distance from the skyrmion center becomes smoother, so that the effective skew scattering is weaker, and on the other the surface where the skew scattering is non zero increases. The normalized scattering asymmetry resulting from our calculations behaves as R^4 indicating that the second mechanism is dominant, and therefore that larger skyrmions yield a stronger Hall signal.

The dependence of the Hall response on the size of the graphene flake is shown in Fig. 4(d), for a fixed radius of $R = 1.4$ nm and an exchange of $J = 80$ meV. We see that by increasing the flake size while keeping the skyrmion radius fixed, the Hall signal decreases as L^{-1} , where L is the linear size of the triangular transmission region. From these results we infer that the Hall conductance behaves as $\mathcal{T}(R, L) \sim R^4/L$ as a function of the radius and of the linear size of the central island. This scaling reflects the fact that the Hall response is proportional to the probability that the electrons surf over the skyrmion, which is manifestly an increasing function of R and a decreasing function of L .

By changing both the radius and the device size by a common factor α , \mathcal{T} scales as $\mathcal{T}(\alpha R, \alpha L) \sim \alpha^3 \mathcal{T}(R, L)$ indicating that the Hall conductance is not scale invariant under simultaneous rescaling of R and L . Now, since we are considering flakes of the minimum experimentally achievable dimensions proximized with the smallest skyrmions experimentally detected so far (of the order of the nm, whereas observation of skyrmions with radius of up to 100 nm has been reported^{15,41}), the presented scaling argument evidences that our estimates of Hall conductances of the order of 10^{-5} - 10^{-4} G_0 merely set a lower bound for the range of values that this parameter can undertake in actual laboratory measurements. A general example of this non-linear scaling trend is shown in fig. 4(e) where a comparison of two systems with L and R scaled by a common factor is presented.

We note that most systems in the brink of hosting skyrmion lattices need a non-zero external magnetic flux to drive them into the skyrmionic phase, as they typically exhibit spiral spin phases at zero magnetic field. This implies that an additional non-zero Hall contribution is to be expected from the external field that sums up to the one driven by the skyrmion alone. An effective way to discriminate between the two effects relies on their different symmetry properties. In fact, while the skyrmionic contribution is electron-hole symmetric (as made clear by

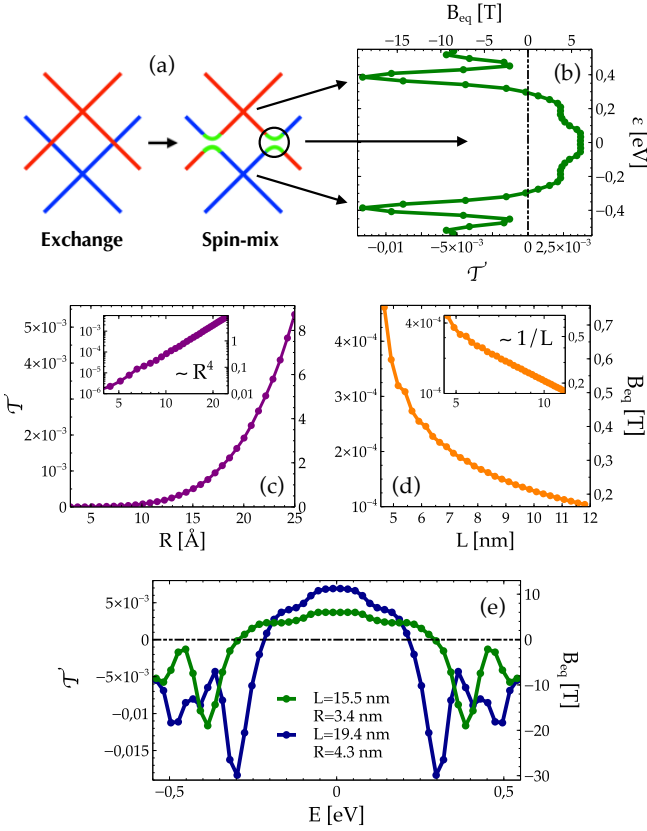


Figure 4. (a) Schematics of the effect on the local electronic structure of graphene of being proximized to a skyrmion. (b) Left-right normalized transmission imbalance \mathcal{T} of a graphene TTD as a function of the transmission energy of the leads ϵ for an island of 15.5 nm, skyrmion radius of 3.4 nm and coupling constant $J = 80$ meV. Energies characterized by maximum absolute Berry curvature in the infinite system are evidenced. (c) and (d) Transmission imbalance of a graphene TTD as a function of skyrmion radius (with fixed flake size of $L = 10.6$ nm) and flake size (with fixed skyrmion radius of $R = 1.4$ nm), respectively. Both calculations have been performed for a coupling constant of 80 meV. Insets show log-log representation of \mathcal{T} . (e) Comparison of two calculations where the radius of the skyrmion and the linear size of the flake are scaled linearly by a common factor $\alpha = 1.25$, for $J = 80$ meV. All plots present a second vertical axis in which the equivalent magnetic field B_{eq} is displayed.

fig. 4(b)) and changes sign only by switching the sign of either J or N , the Hall effect induced by the magnetic field is electron-hole asymmetric as holes have opposite charge with respect to electrons and thus respond with an opposite velocity to an applied external magnetic field. It is thus the $\epsilon \rightarrow -\epsilon$ asymmetry of the overall scattering cross-section that allows to subtract the spurious external contribution and determine the intrinsic skyrmionic one.

B. Effects of disorder

So far we have dealt with a graphene flake perfectly clean. However, some current degradation brought about by defects or impurities in the sample is to be expected. In order to provide a more realistic estimate of the extent to which the Hall responses that our results anticipate are robust with respect to this loss of conductance, we now consider the effect of introducing an amount of scalar disorder in the samples. We do so by averaging over $N = 50$ Anderson disorder configurations in each of which we assign a random scalar on-site potential $W_i \in [-W/2 : W/2]$ to each atom in the quantum dot and tune the parameter controlling the disorder degree W from 0 to a maximum of ~ 400 meV, an upper limit for the energy scale associated with disorder that is consistent with the assumption of Coulomb long-range scattering^{42,43}. The clean limit is recovered for $W = 0$.

We employ square leads and compare two disorder configurations with different symmetry: one where the disorder distribution preserves mirror symmetry with respect to the y axis and one where the distribution is completely random in the whole sample. A realization of each of these different disorder profiles is shown in fig. 5(a,b). Error bars associated with the standard deviation of the data are shown for completeness. From the resulting \mathcal{T}

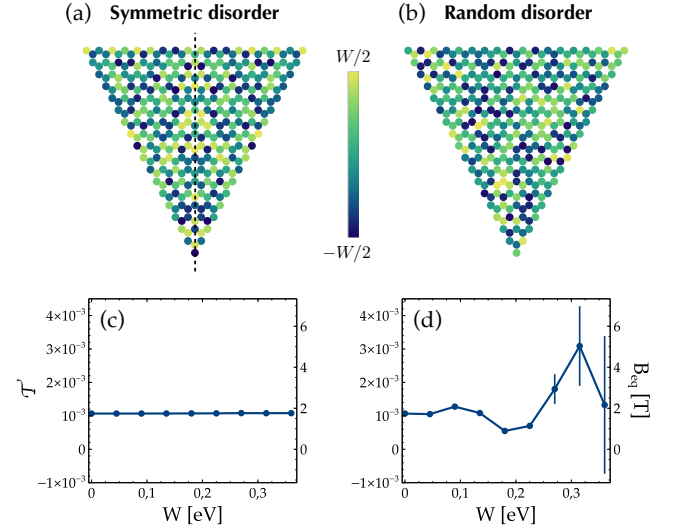


Figure 5. Panels (a) and (b) show a typical realization of a disordered configuration with (a) and without (b) $y \rightarrow -y$ symmetry. In panels (c) and (d) we present the associated curves of \mathcal{T} and B_{eq} as a function of the disorder strength W for fixed values of $J = 80$ meV, $L = 10.6$ nm and $R = 2.3$ nm.

curves shown in fig. 5(c,d) we see that symmetric disorder barely affects the Hall response of the problem, as it provokes changes in the normalized transmission imbalance of the order of $\Delta\mathcal{T}/\mathcal{T} \approx 10^{-2}$. On the other side, a randomly distributed disorder that does not respect $y \rightarrow -y$ symmetry affects the conductance more sizeably,

yielding variations $\Delta\mathcal{T}$ of the order of \mathcal{T} . The difference could be explained by noting that in the symmetric case the defects simply act as a fluctuating potential that does not contribute to the asymmetry of the scattering, whereas in the random case an additional transverse conductance driven by the disorder asymmetry rather than by the skyrmion-induced AHE is generated. However, significant alterations of the Hall response only take place at relatively high values of the disorder potential of the order of ~ 400 meV, whereas for weaker and more reasonable disorder strengths the change in the conductance is smaller and comparable to the one obtained in the symmetric configuration. We can therefore safely rely on the results obtained so far for pristine graphene, as the unavoidable presence of a low concentration of defects and noise in the actual samples is not able to turn down the figure of merit of the problem.

V. CONCLUSIONS

Our results strongly indicate that graphene would be an excellent skyrmion detector at realistic exchange couplings of the order of ~ 1 -10 meV, exhibiting minimum Hall conductances G_H of the order of 10^{-5} - $10^{-4} G_0$, several orders of magnitude larger than the minimum experimentally detectable conductance of the order of $10^{-10} G_0$ ^{44,45}. The equivalent magnetic field B_{eq} can easily reach one Tesla for $J \approx 1$ meV, $R \approx 2$ nm and $L \approx 10$ nm. Besides, these values merely set a lower bound estimate for the conductances that are detectable in actual experimental devices where sample dimensions, skyrmion radius and even skyrmion number can be consistently larger than those considered in this work. Our results also show that at weak coupling Schrodinger electrons are less sensitive to the non-trivial magnetic ordering and respond with a conductance that is some orders of magnitude smaller than that displayed by Dirac electrons. Finally, we proved that scalar disorder does not affect the transverse conductance in a dramatic manner.

In conclusion, we suggest that graphene might be exploited as a non-invasive probe to readout the presence of an individual skyrmion in a material underneath. The underlying physical principle is the enhanced anomalous Hall effect due to the interaction of Dirac graphene fermions with non-coplanar spin textures. Our work establishes the principles of hybrid devices combining graphene Hall probes and insulating skyrmionic materials¹⁰⁻¹².

ACKNOWLEDGMENTS

The authors acknowledge financial support by Marie-Curie-ITN 607904-SPINOGRAPH. JFR acknowledges fi-

nancial supported by MEC-Spain (FIS2013-47328-C2-2-P and MAT2016-78625-C2) and Generalitat Valenciana (ACOMP/2010/070), Prometeo, by ERDF funds through the Portuguese Operational Program for Competitiveness and Internationalization COMPETE 2020, and National Funds through FCT- The Portuguese Foundation for Science and Technology, under the project PTDC/FIS-NAN/4662/2014 (016656). This work has been financially supported in part by FEDER funds. JLL and FF thank the hospitality of the Departamento de Fisica Aplicada at the Universidad de Alicante. We are grateful to F. Guinea and P. San-Jose for useful discussions.

APPENDIX: DETERMINATION OF B_{eq}

In order to determine the equivalent magnetic field B_{eq} , we have performed a calculation of the transmission imbalance \mathcal{T} of a three-terminal triangular device where a perpendicular magnetic field B_\perp is applied to the transmission region. To include such field, we retain only the hopping term of eq. 12 where we perform the standard Peierls substitution $t \rightarrow t \exp\left(-i\frac{e}{\hbar} \int_{\mathbf{r}_i}^{\mathbf{r}_j} \mathbf{A} \cdot d\mathbf{r}\right)$ such that

$$H = -t \sum_{\langle i,j \rangle, \sigma} c_{i\sigma}^\dagger c_{j\sigma} e^{-i\frac{e}{\hbar} \int_{\mathbf{r}_i}^{\mathbf{r}_j} \mathbf{A} \cdot d\mathbf{r}} \quad (19)$$

By calculating the transmission imbalance between left and right lead, one gets a linear relation $\mathcal{T} \approx 20 B_\perp$ as shown in fig. 6. The linear relation between B_\perp and \mathcal{T} , in the absence of a skyrmion, permit to assign an equivalent field B_{eq} to characterize the transmission imbalance calculated in the presence of a skyrmion at $B_\perp = 0$.

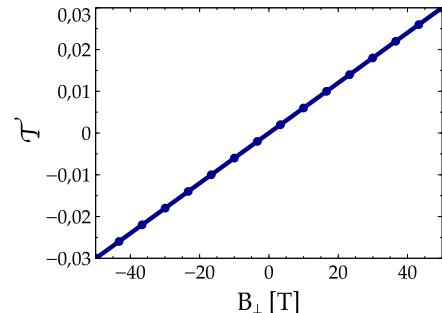


Figure 6. Normalized transmission imbalance $\mathcal{T} = \delta T/T$ as a function of an applied perpendicular magnetic field B_\perp .

- ¹ U. K. Roszler, A. N. Bogdanov, and C. Pfleiderer, *Nature* **442** (2006).
- ² R. Duine, *Nat Nano* **8**, 800 (2013).
- ³ A. Rosch, *Nat Nano* **12**, 103 (2017).
- ⁴ B. Dupé, G. Bihlmayer, M. Böttcher, S. Blügel, and S. Heinze, *Nature Communications* **7**, 11779 EP (2016).
- ⁵ *Nat Nano* **8**, 883 (2013).
- ⁶ S. Mühlbauer, B. Binz, F. Jonietz, C. Pfleiderer, A. Rosch, A. Neubauer, R. Georgii, and P. Böni, *Science* **323**, 915 (2009).
- ⁷ W. Münzer, A. Neubauer, T. Adams, S. Mühlbauer, C. Franz, F. Jonietz, R. Georgii, P. Böni, B. Pedersen, M. Schmidt, A. Rosch, and C. Pfleiderer, *Phys. Rev. B* **81**, 041203 (2010).
- ⁸ X. Yu, N. Kanazawa, W. Zhang, T. Nagai, T. Hara, K. Kimoto, Y. Matsui, Y. Onose, and Y. Tokura, *Nature communications* **3**, 988 (2012).
- ⁹ Y. Tokunaga, X. Yu, J. White, H. M. Rønnow, D. Morikawa, Y. Taguchi, and Y. Tokura, *Nature communications* **6** (2015).
- ¹⁰ S. Seki, X. Yu, S. Ishiwata, and Y. Tokura, *Science* **336**, 198 (2012).
- ¹¹ M. C. Langner, S. Roy, S. K. Mishra, J. C. T. Lee, X. W. Shi, M. A. Hossain, Y.-D. Chuang, S. Seki, Y. Tokura, S. D. Kevan, and R. W. Schoenlein, *Phys. Rev. Lett.* **112**, 167202 (2014).
- ¹² S. Zhang, A. Bauer, H. Berger, C. Pfleiderer, G. van der Laan, and T. Hesjedal, *Applied Physics Letters* **109**, 192406 (2016).
- ¹³ S. Heinze, K. von Bergmann, M. Menzel, J. Brede, A. Kubetzka, R. Wiesendanger, G. Bihlmayer, and S. Blügel, *Nat Phys* **7**, 713 (2011).
- ¹⁴ N. Romming, A. Kubetzka, C. Hanneken, K. von Bergmann, and R. Wiesendanger, *Phys. Rev. Lett.* **114**, 177203 (2015).
- ¹⁵ X. Z. Yu, Y. Onose, N. Kanazawa, J. H. Park, J. H. Han, Y. Matsui, N. Nagaosa, and Y. Tokura, *Nature* **465**, 901 (2010).
- ¹⁶ C. Pfleiderer, *Nat Phys* **7**, 673 (2011).
- ¹⁷ Y. Dovzhenko, F. Casola, S. Schlotter, T. X. Zhou, F. Büttner, R. L. Walsworth, G. S. Beach, and A. Yacoby, *arXiv preprint arXiv:1611.00673* (2016).
- ¹⁸ S. S. Parkin, M. Hayashi, and L. Thomas, *Science* **320**, 190 (2008).
- ¹⁹ F. Jonietz, S. Mühlbauer, C. Pfleiderer, A. Neubauer, W. Münzer, A. Bauer, T. Adams, R. Georgii, P. Böni, R. A. Duine, K. Everschor, M. Garst, and A. Rosch, *Science* **330**, 1648 (2010).
- ²⁰ N. Nagaosa and Y. Tokura, *Nat Nano* **8**, 899 (2013).
- ²¹ K. Hamamoto, M. Ezawa, and N. Nagaosa, *Physical Review B* **92**, 115417 (2015).
- ²² G. Yin, Y. Liu, Y. Barlas, J. Zang, and R. K. Lake, *Physical Review B* **92**, 024411 (2015).
- ²³ J. L. Lado and J. Fernández-Rossier, *Phys. Rev. B* **92**, 115433 (2015).
- ²⁴ N. Nagaosa, J. Sinova, S. Onoda, A. H. MacDonald, and N. P. Ong, *Reviews of Modern Physics* **82**, 1539 (2010).
- ²⁵ J. Brede, N. Atodiresei, V. Caciuc, M. Bazarnik, A. Al-Zubi, S. Blügel, and R. Wiesendanger, *Nature nanotechnology* **9**, 1018 (2014).
- ²⁶ L. Banszerus, M. Schmitz, S. Engels, M. Goldsche, K. Watanabe, T. Taniguchi, B. Beschoten, and C. Stampfer, *Nano letters* **16**, 1387 (2016).
- ²⁷ N. M. Freitag, L. A. Chizhova, P. Nemes-Incze, C. R. Woods, R. V. Gorbachev, Y. Cao, A. K. Geim, K. S. Novoselov, J. Burgdorfer, F. Libisch, *et al.*, *Nano Letters* **16**, 5798 (2016).
- ²⁸ M. B. Shalom, M. Zhu, V. Falko, A. Mishchenko, A. Kretinin, K. Novoselov, C. Woods, K. Watanabe, T. Taniguchi, A. Geim, *et al.*, *Nature Physics* **12**, 318 (2016).
- ²⁹ A. Candini, C. Alvino, W. Wernsdorfer, and M. Affronte, *Phys. Rev. B* **83**, 121401 (2011).
- ³⁰ A. Candini, S. Klyatskaya, M. Ruben, W. Wernsdorfer, and M. Affronte, *Nano Letters*, *Nano Letters* **11**, 2634 (2011).
- ³¹ J. W. González, F. Delgado, and J. Fernández-Rossier, *Phys. Rev. B* **87**, 085433 (2013).
- ³² Z. Qiao, S. A. Yang, W. Feng, W.-K. Tse, J. Ding, Y. Yao, J. Wang, and Q. Niu, *Phys. Rev. B* **82**, 161414 (2010).
- ³³ Ž. V. Šljivančanin, Z. S. Popović, and F. R. Vukajlović, *Physical Review B* **56**, 4432 (1997).
- ³⁴ A. H. Castro Neto, F. Guinea, N. M. R. Peres, K. S. Novoselov, and A. K. Geim, *Reviews of Modern Physics* **81**, 109 (2009).
- ³⁵ R. Landauer, *IBM Journal of Research and Development*, *IBM Journal of Research and Development* **1**, 223 (1957).
- ³⁶ M. L. Sancho, J. L. Sancho, J. L. Sancho, and J. Rubio, *Journal of Physics F: Metal Physics* **15**, 851 (1985).
- ³⁷ P. Wei, S. Lee, F. Lemaitre, L. Pinel, D. Cutaia, W. Cha, F. Katmis, Y. Zhu, D. Heiman, J. Hone, *et al.*, *Nature materials* (2016).
- ³⁸ H. X. Yang, A. Hallal, D. Terrade, X. Waintal, S. Roche, and M. Chshiev, *Phys. Rev. Lett.* **110**, 046603 (2013).
- ³⁹ Z. Qiao, W. Ren, H. Chen, L. Bellaiche, Z. Zhang, A. H. MacDonald, and Q. Niu, *Physical Review Letters* **112**, 116404 (2014).
- ⁴⁰ T. Okubo, S. Chung, and H. Kawamura, *Physical Review Letters* **108**, 017206 (2012).
- ⁴¹ R. Wiesendanger, *Nature Reviews Materials* **1**, 16044 EP (2016).
- ⁴² Z. Wang, C. Tang, R. Sachs, Y. Barlas, and J. Shi, *Phys. Rev. Lett.* **114**, 016603 (2015).
- ⁴³ K. Nomura and A. H. MacDonald, *Physical Review Letters* **98**, 076602 (2007).
- ⁴⁴ A. Tzalenchuk, S. Lara-Avila, A. Kalaboukhov, S. Pao-lillo, M. Syväjärvi, R. Yakimova, O. Kazakova, T. Janssen, V. Fal'Ko, and S. Kubatkin, *Nature nanotechnology* **5**, 186 (2010).
- ⁴⁵ B. Jeckelmann and B. Jeanneret, *Reports on Progress in Physics* **64**, 1603 (2001).